Evolution of a Florida Cirrus Anvil

T. J. GARRETT,[a] B. C. NAVARRO,[a] C. H. TWOHY,[b] E. J. JENSEN,[c] D. G. BAUMGARDNER,[d] P. T. BUI,[c] H. GERBER,[e] R. L. HERMAN,[f] A. J. HEYMSFIELD,[g] P. LAWSON,[h] P. MINNIS,[i] L. NGUYEN,[i] M. POELLOT,[j] S. K. POPE,[k] F. P. J. VALERO,[k] AND E. M. WEINSTOCK[l]

[a] *Meteorology Department, University of Utah, Salt Lake City, Utah*
[b] *College of Oceanic and Atmospheric Sciences, Oregon State University, Corvallis, Oregon*
[c] *NASA Ames Research Center, Moffett Field, California*
[d] *Universidad Nacional Autonoma de Mexico, Mexico City, Mexico*
[e] *Gerber Scientific, Inc., Reston, Virginia*
[f] *Jet Propulsion Laboratory, California Institute of Technology, Pasadena, California*
[g] *National Center for Atmospheric Research,* Boulder, Colorado*
[h] *SPEC, Inc., Boulder, Colorado*
[i] *NASA Langley Research Center, Langley, Virginia*
[j] *Department of Atmospheric Sciences, University of North Dakota, Grand Forks, North Dakota*
[k] *Scripps Institution of Oceanography, La Jolla, California*
[l] *Harvard University, Cambridge, Massachusetts*

(Manuscript received 6 April 2004, in final form 1 November 2004)

ABSTRACT

This paper presents a detailed study of a single thunderstorm anvil cirrus cloud measured on 21 July 2002 near southern Florida during the Cirrus Regional Study of Tropical Anvils and Cirrus Layers–Florida Area Cirrus Experiment (CRYSTAL-FACE). NASA WB-57F and University of North Dakota Citation aircraft tracked the microphysical and radiative development of the anvil for 3 h. Measurements showed that the cloud mass that was advected downwind from the thunderstorm was separated vertically into two layers: a cirrus anvil with cloud-top temperatures of −45°C lay below a second, thin tropopause cirrus (TTC) layer with the same horizontal dimensions as the anvil and temperatures near −70°C. In both cloud layers, ice crystals smaller than 50 μm across dominated the size distributions and cloud radiative properties. In the anvil, ice crystals larger than 50 μm aggregated and precipitated while small ice crystals increasingly dominated the size distributions; as a consequence, measured ice water contents and ice crystal effective radii decreased with time. Meanwhile, the anvil thinned vertically and maintained a stratification similar to its environment. Because effective radii were small, radiative heating and cooling were concentrated in layers approximately 100 m thick at the anvil top and base. A simple analysis suggests that the anvil cirrus spread laterally because mixing in these radiatively driven layers created horizontal pressure gradients between the cloud and its stratified environment. The TTC layer also spread but, unlike the anvil, did not dissipate—perhaps because the anvil shielded the TTC from terrestrial infrared heating. Calculations of top-of-troposphere radiative forcing above the anvil and TTC showed strong cooling that tapered as the anvil evolved.

1. Introduction

The anvil cirrus outflow from low-latitude cumulonimbus clouds is an important component of the earth's climate for its role in moistening the upper troposphere and its perturbation to atmospheric fields of solar and terrestrial radiative fluxes. There is an increasing realization that numerical simulations of low-latitude climate require implementation of detailed cloud microphysics schemes (e.g., Iacobellis and Somerville 2000). However, there have been relatively few in situ measurements that can be used to guide these computations. This is largely due to the logistic difficulties associated with flying aircraft in low-latitude anvil cirrus: these clouds are high, cold, and often remote.

* The National Center for Atmospheric Research is sponsored by the National Science Foundation.

Corresponding author address: Dr. T. J. Garrett, Meteorology Dept., University of Utah, 135S 1460E, Rm. 819, Salt Lake City, UT 84112.
E-mail: tgarrett@met.utah.edu

The few airborne studies of low-latitude cirrus anvils (Griffith et al. 1980; Knollenberg et al. 1982; 1993; McFarquhar and Heymsfield 1997; Heymsfield et al. 1998) have shown, for example, that low-latitude cirrus anvil ice water content (IWC) is horizontally variable, decreases with increasing height, and can range from a few hundredths of a gram per cubic meter to over a tenth of a gram per cubic meter; due to ice crystal sedimentation and aggregation, large ice crystals are most common near the base of an anvil, where sizes larger than 1000 μm are not uncommon; near the anvil top, concentrations of ice crystals with sizes smaller than $<$100 μm might exceed 100 cm^{-3}; and large precipitating crystals near cloud base contribute most highly to the solar albedo of the cloud.

However, these early studies had several limitations. In most, fields of cloud mass and optical extinction were not measured directly but rather estimated from integration of ice crystal size distributions. Although this was unavoidable given the available instrumentation, such integration required some simplistic assumptions about crystal habit and density. Also, either instrument uncertainty or lack of instrumentation limited confident measurement of the concentrations of ice crystals smaller than approximately 50-μm diameter. And aircraft were often unable to reach the extreme upper portions of low-latitude anvils where ice crystals tend to be smallest, and where they are most radiatively important due to their more direct exposure to outer space. Finally, anvils clearly develop as they detrain from convection, but in none of these studies was this evolution probed in detail.

This paper attempts to address these limitations using data obtained during the Cirrus Regional Study of Tropical Anvils and Cirrus Layers-Florida Area Cirrus Experiment (CRYSTAL-FACE), which focused on anvil cirrus over southern Florida. The dataset allowed a detailed case study of the evolution of a single low-latitude cirrus anvil sampled over 3 h on 21 July 2002. The anvil was chosen from others studied during CRYSTAL-FACE because it was isolated from surrounding convection and it was well characterized by two aircraft in situ. The aircraft were outfitted with an unusually wide range of microphysical, meteorological, and radiation probes, many of which were flown in anvil cirrus for the first time.

2. Meteorological overview

A thunderstorm formed over the west coast of Florida in the afternoon of 21 July 2002. No significant synoptic systems were in the storm development region. Instead, diurnal heating over the peninsula and general light southerly low-level flow enabled a north to south sea-breeze front to develop over the west coast of Florida by early afternoon. This sea-breeze front is evident on satellite images centered on the storm development region (Fig. 1a). Nearby soundings showed values of convective available potential energy (CAPE) near 1000 J kg^{-1}. This CAPE value is only about half the mean value of 2500 J kg^{-1} found in the region during the latter half of CRYSTAL-FACE. However, it is within 15% of mean values observed during other low-latitude field campaigns such as the Tropical Ocean and Global Atmosphere Coupled Ocean–Atmosphere Response Experiment (TOGA COARE), which took place over the western Pacific Ocean warm pool, and within the range of 660–1190 J kg^{-1} measured for GATE, which took place over the tropical Atlantic (Li 2003). Low-level convergence along the sea-breeze front combined with the convective instability to initiate storm development over the southwest Florida peninsula at about 1700 UTC, with anvil development occurring subsequently at about 1815 UTC (Fig. 1b). A sounding was taken on Florida's west coast at 25°53′N, 81°19′W, ~12 km west of the sea-breeze front and ~35 km southeast of the storm development location. The sounding indicates the region was characterized by 15 to 20 m s^{-1} northeasterly winds at 200 hPa (Fig. 2). Consequently, the anvil trajectory at this level was to the southwest over the open waters of the Gulf of Mexico and in the opposite direction of the movement of the storm (Fig. 1c). The storm reached a peak intensity at 1750 UTC, with radar reflectivities near 50 dBZ, and remained near peak intensity until 1840 UTC when it began to weaken. Most of the resulting cloud mass then relaxed to what was presumably its level of neutral buoyancy at about 11-km altitude. National Aeronautics and Space Administration (NASA) S-band polarimetric radar (N-POL) imagery showed an outflow boundary nearer the surface that propagated to the east away from the storm, and peak reflectivities decreased to less than 40 dBZ. Meanwhile, the anvil spread southwest over the gulf, and, by 1945 UTC, it separated from the dissipating storm.

3. Measurement techniques

a. Airborne platforms

The majority of the aircraft measurements were carried out during the dissipating stages of the storm between 1945 and 2145 UTC, with a few measurements taken while the anvil was still developing between 1845

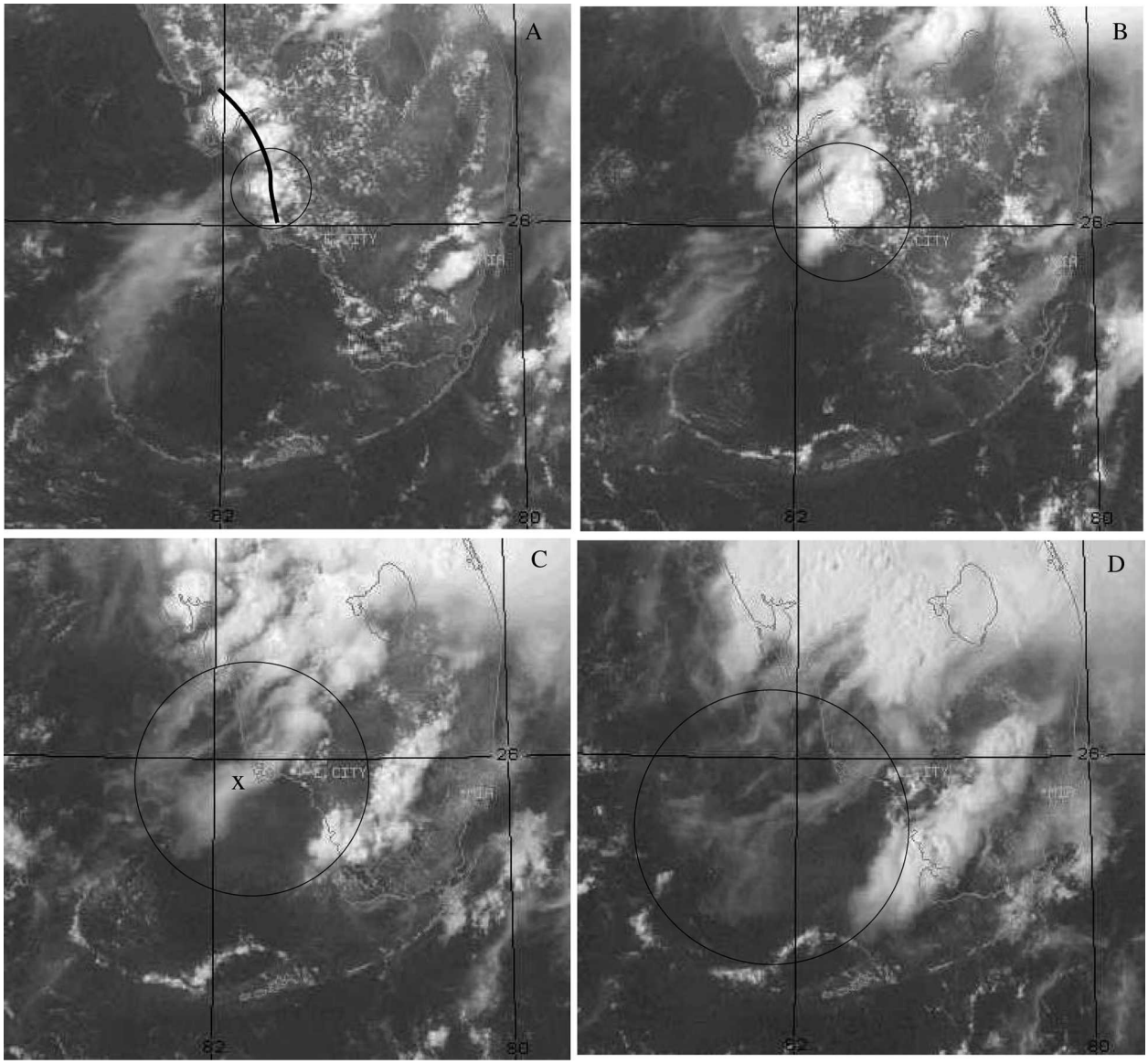

FIG. 1. Visible *GOES-8* images over southern Florida for the period from (a) 1745 to (d) 2045 UTC in 1-h increments. The circle denotes the storm/anvil of interest. The thick line in (a) marks the location of the sea-breeze front, which caused the low-level convergence that generated the storm. The "x" in (c) denotes the approximate location of the spiral ascents completed by the aircraft.

and 1945 UTC. Measurements were closely representative of a single system since the storm was sufficiently small to be isolated from adjacent convection. In this study, only data from instruments mounted on the NASA WB-57F and the University of North Dakota (UND) Citation Cessna II aircraft are used. Maximum altitudes attained by each aircraft on 21 July were ~15.7 and ~12.0 km, respectively, while the average flight airspeed of both aircraft was ~140 m s^{-1}. Specific instruments located on each aircraft are discussed in the following section.

b. Instrumentation

1) ICE CRYSTAL SIZES AND SHAPES

On the Citation, a Particle Measuring Systems, Inc. (PMS) forward scattering spectrometer probe (FSSP-100), a PMS optical array probe (OAP) 2D-C cloud probe, and a Stratton Park Engineering Company, Inc. (SPEC) high-volume precipitation spectrometer measured the combined size range of ice crystals from 4 to 27 000 μm in diameter. Aboard the WB-57F, a Droplet Measurement Technologies, Inc., cloud aerosol precipi-

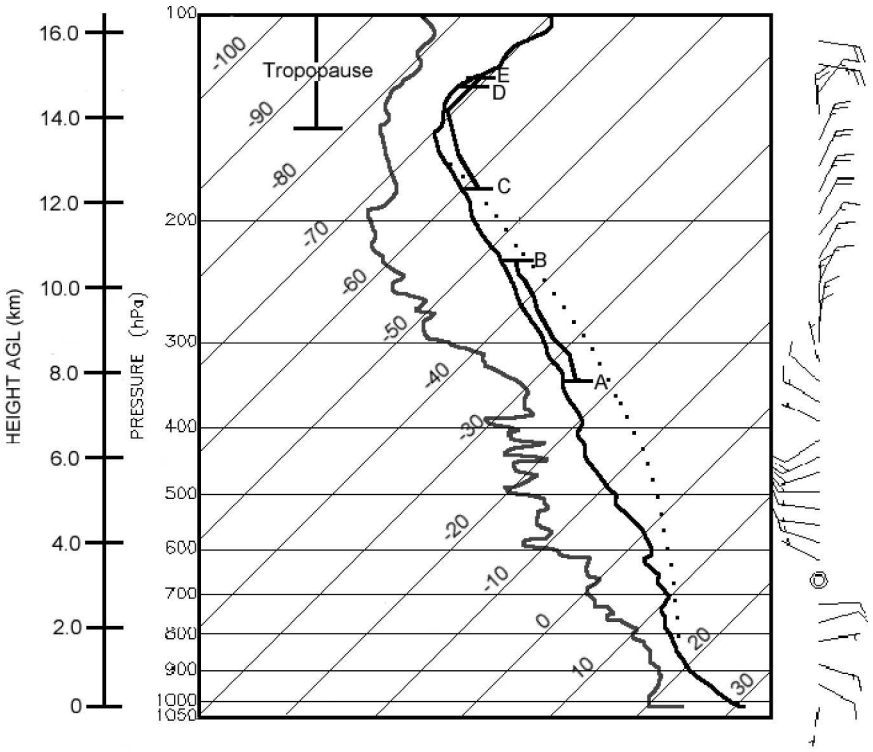

FIG. 2. Skew T–log$p$ diagram of a temperature (black) and dewpoint (gray) sounding taken at 25°53′N, 81°19′W at 1725 UTC 21 Jul 2002. Heavy lines to the right of the temperature profile denote temperatures observed during vertical profiles by the NASA WB-57F and UND Citation during a profile through thin tropopause cirrus and a cirrus anvil. Approximate height, using a scale height of 7.2 km estimated from raw height coordinates from the radiosonde, is shown to the left of the pressure scale; A denotes the base of the anvil, B is the top of the anvil, and C and D denote the base and top of the thin tropopause cirrus, respectively. The maximum height of the WB-57F during the vertical profile is shown by E. The dotted line represents saturated surface parcel ascent for $\theta_e = 296$ K.

tation spectrometer (CAPS) was used to measure size distributions of particles between 0.5 and 1550 μm in diameter (Baumgardner et al. 2002). The CAPS probe is actually a combination of the cloud aerosol spectrometer (CAS, which sizes particles smaller than 50 μm) and the cloud imaging probe (CIP, which images particles larger than 25 μm). The CAS works on principles similar to the FSSP-100, and the CIP is similar to the OAP 2D-C, except that it has an extended size range and updated electronics.

Since the 2D-C has a restricted sample volume for small crystal sizes, FSSP-100 data are used in this study for the size range between 25 and 62 μm covered by both instruments. Ice crystals between 10 and 500 μm were imaged on both aircraft using a SPEC cloud particle imaging probe (CPI; Lawson et al. 2001), which has a nominal 2.5-μm resolution. In the CPI, ice crystals pass through an intersection of two lasers. The instrument then images the ice crystal with a third laser pointed toward a digital camera.

2) BULK MICROPHYSICAL PROPERTIES

Bulk microphysical probes on the Citation and WB-57F did not measure individual ice crystals, but instead the integral properties of ice crystal populations. The three bulk quantities measured on both aircraft were the optical extinction coefficient β_{ext}, IWC, and the asymmetry parameter g. Measurements of β_{ext} and g are used in radiative transfer models to estimate cloud radiative fluxes. The value of g indicates the degree of forward versus backscattering by ice crystals, while β_{ext} represents the optical cross-sectional density. It is more simple, and ostensibly more accurate, to obtain the bulk quantities g, β_{ext}, and IWC from bulk probes rather than from size distributions of cross-sectional areas, habits, and densities of individual ice crystals: fewer assumptions about ice crystal shape are required.

Both the Citation and WB-57F used a Gerber Scientific, Inc., cloud integrating nephelometer (CIN; Gerber et al. 2000) to measure β_{ext}. The CIN detects 635-nm

laser light scattered by ice crystals into four integrating Lambertian sensors covering an angular domain of 10°–175°. The fraction of light f scattered outside the CIN angular domain is estimated to be 0.57 with an uncertainty of ±0.02 due to variability in crystal habit (Gerber et al. 2000). The value of f is closely constrained because forward diffraction is one-half of scattered energy by particles large with respect to the wavelength of light, independent of their particle shape. Both CINs had large sampling volumes of ~0.5 $m^3 s^{-1}$. The lowest value of β_{ext} reliably detected was approximately 0.4 km^{-1} aboard the WB-57F and about 1.0 km^{-1} aboard the Citation, but with approximately 40% error due to extraneous light leakage and photomultiplier shot noise. In clouds approximately twice as optically thick, the error is estimated to be about 15% based on calibration uncertainties, uncertainty in f, and noise (Garrett et al. 2001). The CIN aboard the Citation obtained the asymmetry parameter g at visible wavelengths with an estimated uncertainty of ±0.02 in clouds where $\beta_{ext} > 10$ km^{-1}.

Bulk IWC was obtained using a Harvard Lyman-alpha total water probe aboard the WB-57F and a counterflow virtual impactor (CVI) aboard the Citation. The Harvard Lyman-alpha total water instrument uses an inlet heater to evaporate ice crystals and a 121.6-nm radiation lamp to photodissociate water vapor. The fluorescence of the resulting hydroxyl (OH) molecules, detected in a photomultiplier tube, is proportional to the water-vapor volume mixing ratio. Ice water content is then derived by subtracting out water vapor from total water. A full description of this instrument has been given in Weinstock et al. (1994). The CVI impacts cloud ice crystals and water drops into dry nitrogen gas, where the crystals and drops evaporate (Noone et al. 1988). The water vapor resulting from the evaporating drops and ice crystals is then measured using a Lyman-alpha absorption hygrometer (Buck 1985; Twohy et al. 1997). The estimated accuracy for both measurements of IWC is approximately 15%.

In the past, the ice crystal effective radius r_e, which is important in radiative transfer calculations for parameterizing cloud scattering and absorption, has normally been derived from measurements of ice crystal size spectra. This requires assumed mass, area, and length relationships for ice crystals. Here we circumvent these issues by using direct measurements of β_{ext} and IWC, from which r_e is derived using

$$r_e = \frac{3\text{IWC}}{2\rho_i\beta_{ext}} \quad (1)$$

(Foot 1988; Garrett et al. 2003), where ρ_i is the bulk density of ice. Equation (1) is general for all possible distributions of ice crystal shape and size.

3) METEOROLOGICAL AND SATELLITE MEASUREMENTS

Aboard the WB-57F, meteorological state variables, such as temperature, pressure, and wind velocity were measured using the Meteorological Measurement System (Scott et al. 1990). Relative humidity was measured using the Jet Propulsion Laboratory (JPL) laser hygrometer (May 1998). The JPL laser hygrometer uses a near-infrared diode laser to detect water vapor. On the Citation, temperature and pressure were measured with a Rosemount total temperature probe (Payne et al. 1994) and a Rosemount static pressure transducer. Wind velocity was obtained using the Citation's airspeed, ground speed, and the aircraft's position and orientation system (Khelif et al. 1999). Relative humidity measurements were obtained using a tunable diode laser (TDL). The estimated accuracy of the TDL is 5%.

Broadband flux for the shortwave and infrared radiative fields was measured aboard the WB-57F using the Radiation Measurement System (Valero et al. 1997). This system uses radiometers to measure both upwelling and downwelling radiation.

In addition to the airborne instruments, this study uses *Geostationary Operational Environmental Satellite* (*GOES*)*-8* visible and infrared solar infrared split window technique (VISST)-derived cloud products matched to the flight tracks of each aircraft (Minnis et al. 1995, 1998). These products are derived from a weighted average of the four closest pixels to the aircraft position.

c. *Aircraft flight patterns*

Aircraft flight patterns were coordinated so that the WB-57F sampled the extreme upper portions of the anvil while the Citation sampled the middle and lower portions. Nine level flight legs were completed by the WB-57F, and six were completed by the Citation (Fig. 3). The WB-57F flew across the anvil axis for legs 1–3 and then along most of the length of the anvil axis at an angle of about 35° for the remainder of the legs. The Citation flew at an angle of approximately 35° to the anvil axis, stopping in the center portion of the anvil.

In addition to the horizontal transects, a spiral ascent profile was completed by each aircraft (Fig. 1c), with the WB-57F displaced about 15 km to the southwest of the Citation. The Citation's maximum altitude for the vertical profile was about 11.3 km while the WB-57F profile extended from 12.9 to 15 km. Thus, an approxi-

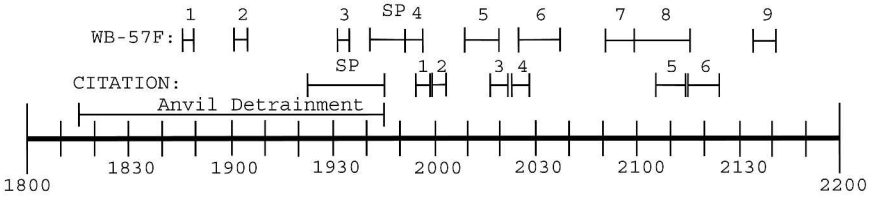

FIG. 3. Timeline (UTC) of the numbered flight legs completed by the NASA WB-57F and UND Citation on 21 Jul 2002 while sampling the evolution of an individual anvil (Fig. 1). Here SP refers to the spiral vertical profile completed by each aircraft. The period associated with detrainment of the anvil from the storm is estimated from *GOES-8* imagery. The anvil detached from the storm at 1945 UTC. Initial development of the storm occurred at approximately 1650 UTC.

mate vertical gap of 1.6 km separated the upper profiles of the two planes. This gap makes it difficult to ascertain with certainty the total depth of the cloud. However, flight notes from the WB-57 remarked on the presence of two cloud layers. Also, the *GOES-8* retrieved a cloud-top height of ~11.0 km for the anvil, which is similar to the maximum cloud height of 11.3 km measured by the Citation. This suggests the Citation profiled the entire vertical depth of a cloud layer, which we call the anvil proper, that was distinct and much thicker than a higher cloud layer sampled by the WB-57F. We believe this second layer sampled by WB-57F during legs 4–9 was separated vertically from the anvil proper by more than 1 km. The exact origin of this tropopause cloud is not clear. However, based on satellite retrieved cloud-top height and N-POL radar time–height cross sections, it appears the WB-57F sampled near the storm's second convective impulse at its highest altitude of 14–15 km during legs 1–3, but then most of the cloud mass was detrained further below, presumably at the level of neutral buoyancy. Either cloudy air or the moist precursors to cloud were detrained or formed at ~14 km altitude, where equivalent potential temperature θ_e values were within ± 2 K of those measured within the convective impulse. We do not believe this cloud was advected over the storm anvil from another location; horizontal transects through the tropopause layer showed that it had nearly identical horizontal dimensions to the anvil beneath it. Since this feature was observed above anvils on other days during CRYSTAL-FACE, we hereinafter refer to this upper-cloud layer as thin tropopause cirrus (TTC), while the thicker lower cloud is referred to as the anvil.

4. Microphysical and single-scattering properties

a. Vertical profile

Measurements of microphysical and radiative parameters obtained during the vertical profile of the TTC and anvil are shown in Figs. 4 and 5, respectively. At the time of the profile, the anvil was still attached to the convective core.

Shown size distributions are normalized by total concentration in order to clarify differences in the shape of the size distribution. Within the TTC the size distribution was monomodal, and the particles measured did not usually exceed 100-μm maximum dimension (hereinafter ice crystal sizes will be expressed in terms of maximum dimension unless otherwise stated) and the mode size in the number distribution was located at about 20 μm. CPI images showed a few columns, spheres, and irregularly shaped ice crystals, with most of the columns and spheres found at the bottom of the TTC (Fig. 6).

For the majority of the profile, the relative humidity was well above ice saturation, reaching a maximum value of ~150% in the middle of the cloud, as compared with ~100% in ambient clear air. This is where ice crystals were smallest, which suggests that haze aerosols in the layer were actively freezing homogeneously to form new ice crystals. The TTC was very tenuous with total ice crystal concentrations usually below 500 L^{-1} and an average IWC of 0.001 25 g m^{-3}. Through the depth of the profile, the vertically integrated ice water content, or ice water path (IWP), was ~1.5 g m^{-2}.

Optical properties of the layer are shown in Fig. 5b. Values of β_{ext} in the TTC were consistently below the CIN lower detection threshold of 0.4 km^{-1}, and so extinction, effective radius and visible optical depth are estimated from CAPS data, assuming spherical particles over the CAS size range. In thicker clouds measured during CRYSTAL-FACE, CIN measurements of β_{ext} were usually highly correlated but 30%–40% higher than estimates from the CAPS probe, which is within experimental uncertainty (Garrett et al. 2003). CAPS cumulative optical depth τ for the cloud was 0.2 while values of β_{ext} were at or below 0.2 km^{-1}

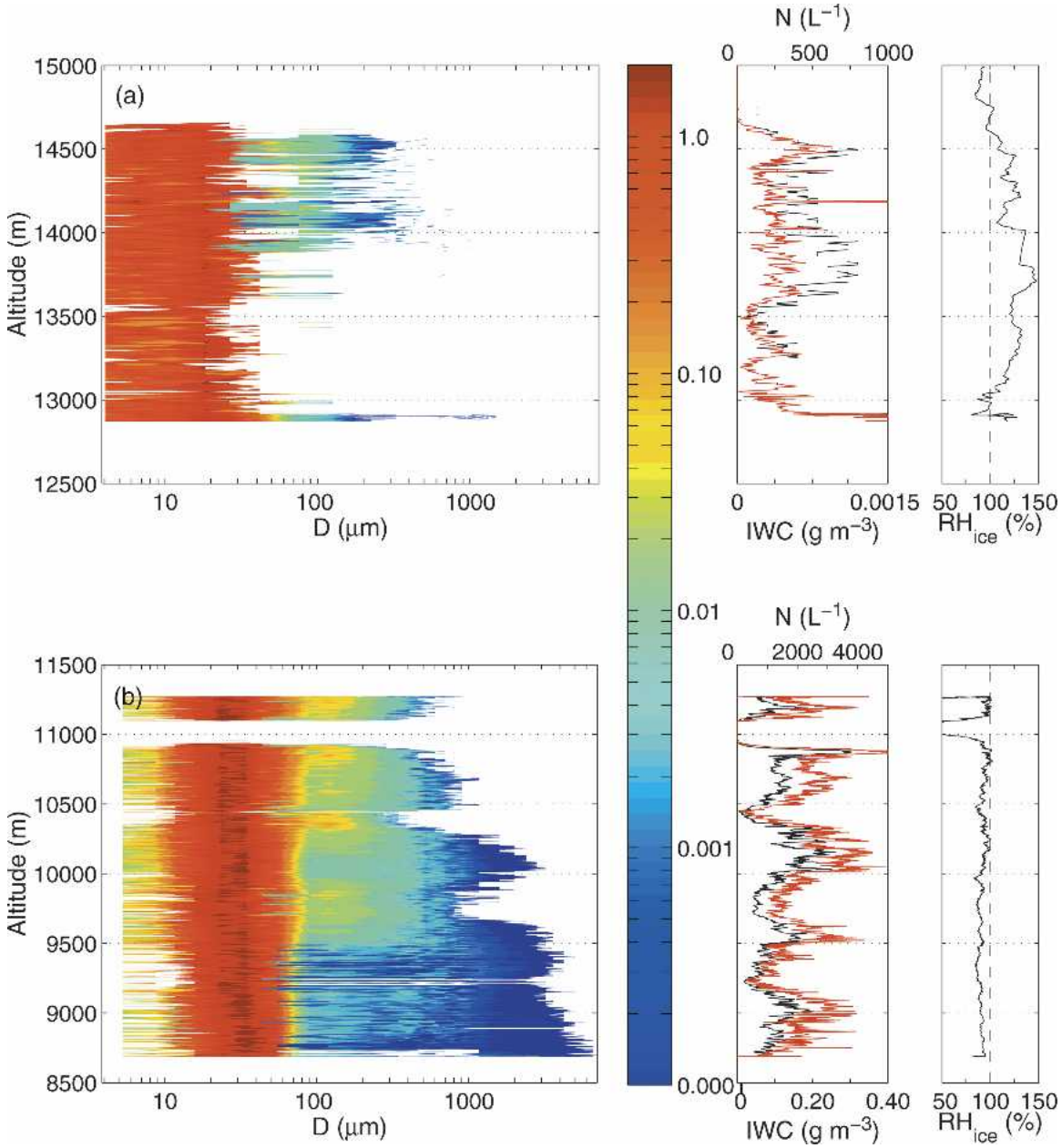

FIG. 4. Vertical profile of size distributions normalized by total concentration [$(dN/d\log D)/N$], total cloud crystal concentration N (red line), IWC (black line), and relative humidity with respect to ice RH_{ice} in (a) the thin tropopause cirrus and (b) the anvil sampled by the WB-57F and Citation, respectively, on 21 Jul 2002.

throughout the cloud's depth, with values for r_e of ~10 μm.

The anvil proper was 1.5 h old when it was profiled vertically by the Citation. Considering this particular storm was not particularly strong compared to others measured during CRYSTAL-FACE, maximum values of IWC in the profile were very high, reaching 0.30 g m^{-3} over much of the profile. Above 9500-m altitude, size distributions had two modes, located at ~30- and ~105-μm maximum dimension. Below 9500-m altitude, the larger mode was absent. In situ and atmospheric sounding data (Fig. 2) showed that below this level winds also shifted, from 5 m s^{-1} northwesterly to 10 m s^{-1} northeasterly. It is unclear what the influence of different ice crystal trajectories might be on the size distribution. Assuming the smaller cloud mode was composed of solid ice spheres, it contributed approximately 20% to total IWC over the depth of the anvil.

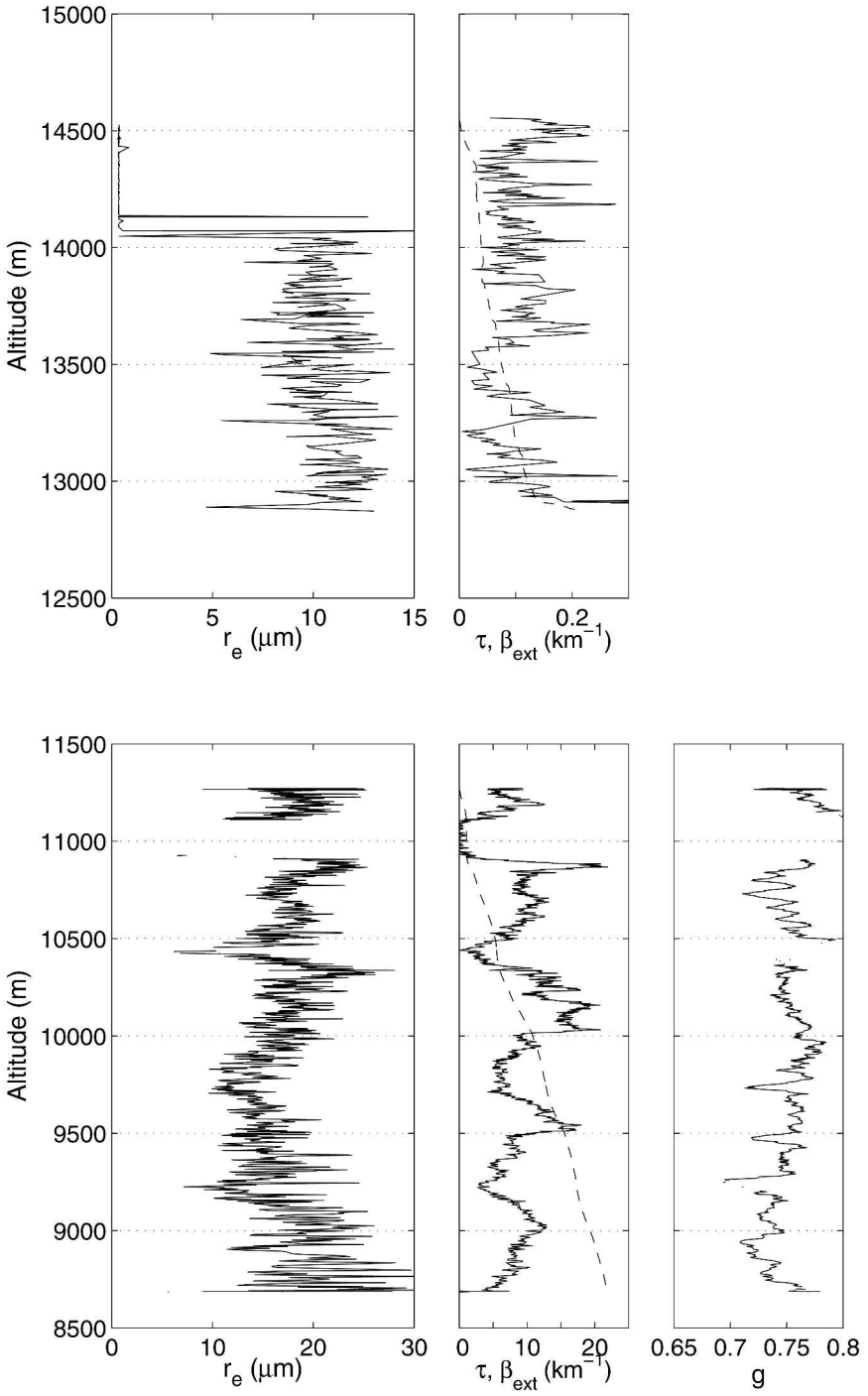

FIG. 5. As in Fig. 4, but for effective radius r_e, visible extinction β_{ext}, accumulated visible optical depth τ measured from cloud top (dashed), and asymmetry parameter g. The effective radius, extinction, and optical depth plotted in the top panels are derived from the CAPS probe. The measurements in the bottom panels are derived from the CVI and CIN probes. Optical depth τ is derived from vertically integrating β_{ext}.

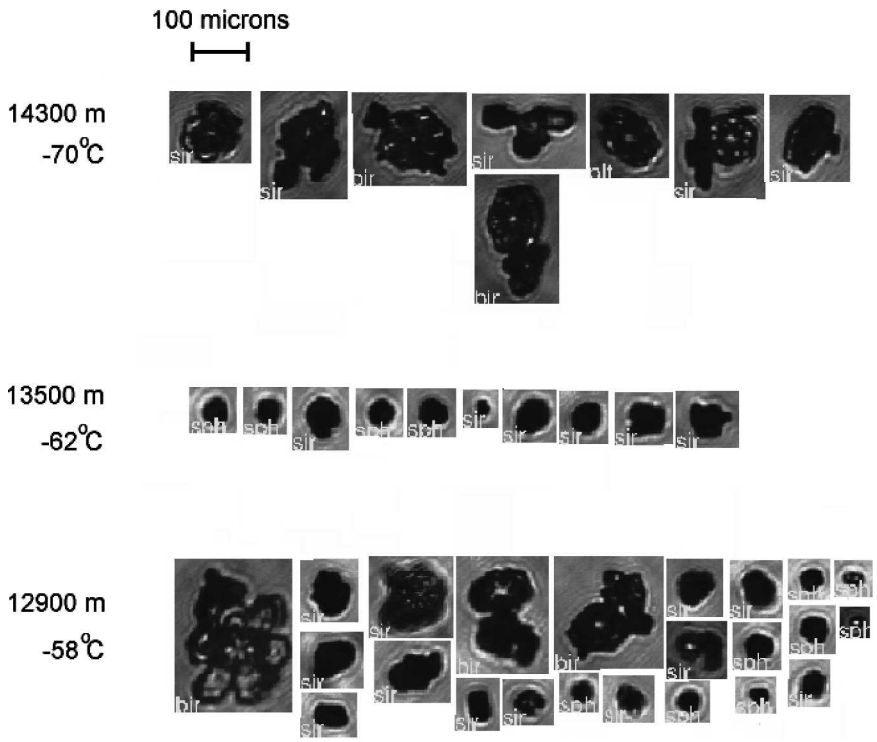

FIG. 6. CPI images of crystal habits encountered during the WB-57F vertical profile within the thin tropopause cirrus.

Vertical fluctuations in IWC and total cloud crystal concentration N in Fig. 4b are probably seen because the Citation repeatedly flew across a horizontal gradient in cloud density with each successive turn in the spiral ascent. This variability aside, IWC and N are surprisingly uniform vertically. This contrasts with earlier measurements in low-latitude thunderstorm anvils, which have generally shown smaller values of IWC near cloud top (e.g., Heymsfield 1986).

Figure 5b, shows a profile of the measured cloud optical properties. The extinction coefficient was also relatively uniform with height, and highly correlated with IWC and N. Mean values of β_{ext} were approximately 10 km^{-1}. The cumulative visible optical depth τ and ice water path IWP for the layer derived from in situ measurements of β_{ext} and IWC were 21.7 and 240 g m^{-2}, respectively. Values of the asymmetry parameter g measured in the anvil were about 0.74, which is approximately what has been found theoretically for idealized fractal ice crystals (Macke 1993) and what has been measured within cirrus in the Arctic (Garrett et al. 2001).

The effective radius [Eq. (1)] in the upper 1500 m of the anvil was approximately 18 μm, gradually increasing from 9500-m altitude to 25 μm in the 1000 m below. The location of this transition corresponds roughly with the beginning of a 150-μm precipitation mode in the ice crystal size distribution (Fig. 4b). Below this level, this precipitation mode was absent, but very large ice crystals >1000 μm became increasingly prevalent. Apparently, these very large ice crystals contributed only to a rather modest increase in r_e of ~50% at cloud base. CPI images also showed these large crystals were primarily aggregates of plates that had undergone varying degrees of evaporation as they fell (Fig. 7). Small crystals of less than 50 μm in diameter, found mostly near cloud top, were quasi-spherical in shape. A few pristine hexagonal plates were also observed.

The relative humidity in the anvil was near or below ice saturation for the majority of the profile (Fig. 4b), as compared with ~60% in ambient clear air. Since high supersaturations with respect to ice are required for ice production due to homogeneous freezing of haze particles (Koop et al. 2000), homogeneous nucleation of any new ice crystals from haze particles had probably ceased at the level of flight measurement. In this case, the observed ice crystals were likely either ejected from the storm updraft or formed near the anvil base and lofted upward.

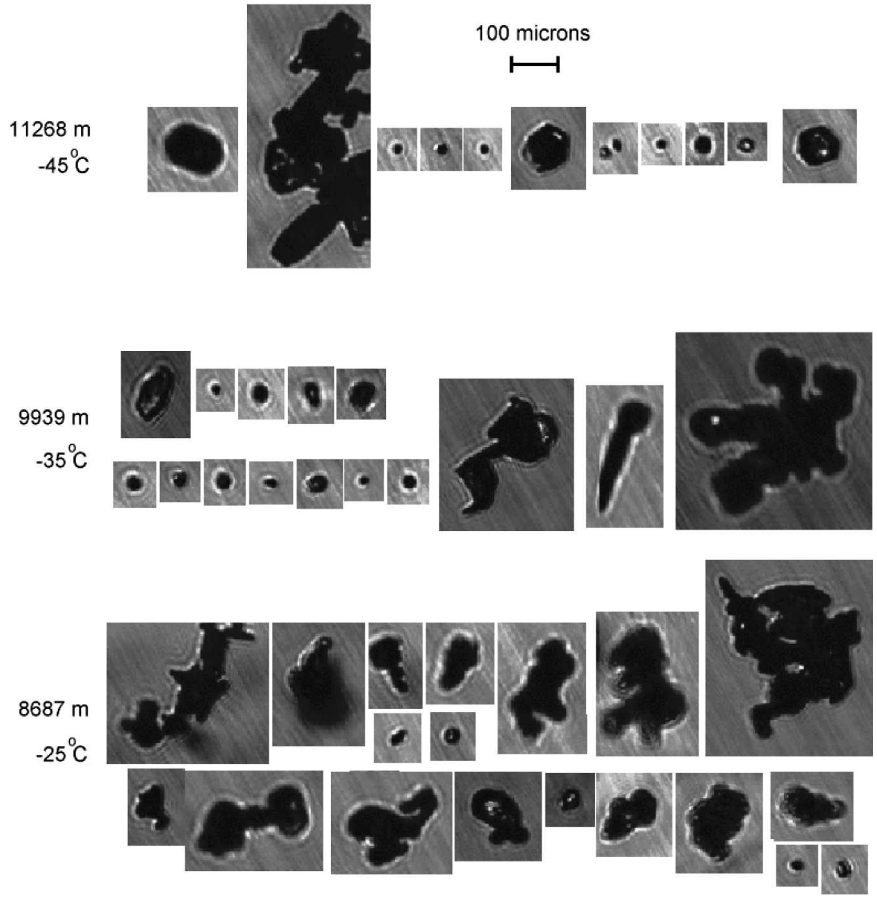

FIG. 7. CPI images showing the crystal habits encountered during the Citation vertical profile within the anvil.

b. Horizontal transects

During the period of strong convection, while the anvil was forming, the WB-57F sampled the storm cloud along a southeast–northwest trajectory across the anvil's downwind axis. Following anvil separation from the storm, flight legs were flown along the anvil's axis (Fig. 3). The Citation flew only along-axis transects, in coordination with the WB-57F. Combined, the transects from the two aircraft paint a picture of the evolution of cloud microstructures in the TTC and anvil.

1) ACROSS AXIS

During legs 1–3 the WB-57F sampled cloud across-wind approximately 20 km downwind of the core of a thunderstorm convective impulse that reached maximum intensity at 1840 UTC, according to N-POL radar imagery. Ice crystal size distributions measured during these legs are shown in Fig. 8. Leg 1 was at 14.7-km altitude, followed by legs 2 and 3 in descending 600-m intervals.

The shapes of the number size distributions were similar in each case, with comparatively high concentrations of large crystals (Fig. 8). A single mode, located at ~20 μm, was found at each altitude, and the slope of the size distribution was ~3 for ice crystals smaller than 200 μm and less than 1 for ice crystals larger than 200 μm (Fig. 8). That a few large ice crystals were present suggests the TTC cannot have formed entirely from in situ homogeneous nucleation, but rather at least some portion must have come from the deep convection.

The bulk of the storm's second convective impulse at 1840 UTC was not sufficiently strong to reach 14.7-km altitude. Average N, IWC, and β_{ext} values at 14.7-km altitude were about 1/20 of those measured just 15 min later at 14.1-km altitude (Table 1). Average N, IWC, and β_{ext} at 14.1 km were 10.7 cm^{-3}, 0.035 g m^{-3}, and 9.0 km^{-1}, respectively, which is remarkably high considering measurements were made just a few hundred meters below the tropopause. Cloudy air at 1930 UTC and 13.5-km altitude (leg 3) was again very tenuous.

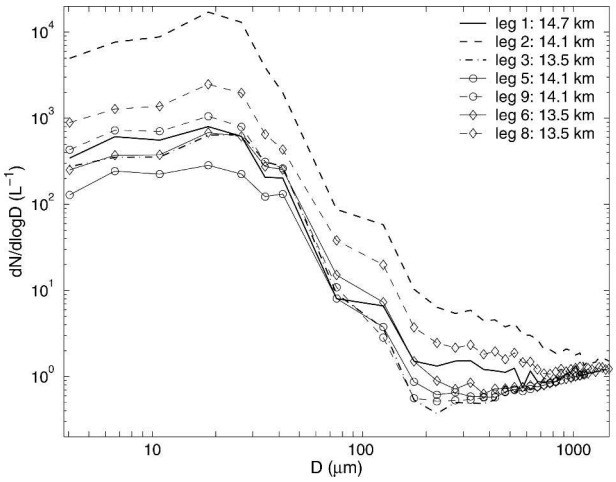

FIG. 8. Average ice crystal size distributions near the tropopause 20 km downwind from a convective impulse that reached its peak at 1840 UTC. Measurements were obtained aboard the WB-57F during legs 1–3 (Fig. 3).

Thus, it is possible the thick cloud measured during leg 2 spread to become the tenuous TTC layer.

2) ALONG AXIS

The TTC had a single mode in the ice crystal size distribution, located at ~20 μm, independent of altitude, cloud age, or distance from the cloud's upwind edge and had few crystals larger than 200 μm (Fig. 8). Further there were no discernible spatial trends in IWC, N, and β_{ext}. The average altitude, age, temperature, N, IWC, β_{ext}, r_e, and RH at 14.1-km altitude (legs 5 and 9) and 13.5-km altitude (legs 6 and 8) are listed in Table 1. Average age represents the approximate flight leg–averaged age of the cloud mass, relative to its time of initial detrainment from the convective updraft, as determined from satellite imagery. At 14.1-km, average N decreased by 78% over 50 min of evolution; at 13.5 km, N increased by 210% over 25 min of evolution. The effective radius and relative humidity showed no dependence on either altitude or age, but the temperature at each altitude warmed by 1°C. Thus, rather than dissipating, the cloud appears to have been slowly subsiding. The relative humidity within the TTC consistently remained above ice saturation during its evolution. Plausibly the effective radius remained at about 6 μm (Table 1), despite the supersaturated conditions, because of a close balance between Maxwellian growth of small crystals and sedimentation of large crystals.

In contrast to the TTC, the anvil was characterized by a distinct bimodal ice crystal size distribution (Fig. 9). The cloud mode was centered at about 25 μm and changed with neither distance downwind from the anvil leading edge nor anvil age. At approximately 1-h age (leg 3), the precipitation mode, centered near 150 μm at the upwind edge of the anvil, increased in size over an approximate 30-km distance downwind to 700 μm at the anvil's downwind edge. This size shift with distance was not as evident at the same altitude 60 min later (leg 5), but rather remained at a constant mode size of about 150 μm.

Averaged over all Citation legs 1–6, IWC, N, RH, β_{ext}, and r_e were highest at the upwind edge of the anvil, and decreased as distance increased downwind (Fig. 10). The relative humidity became progressively subsaturated downwind from the anvils leading edge, decreasing from 95% to ~60% over a distance of 35 km. Measurements of g had a high level of uncertainty, since the extinction was relatively low. However, values remained approximately uniform over the length of the anvil.

At an altitude of 11.2 km (legs 1 and 6), which was near the top of the anvil, N, IWC, and β_{ext} fell by about 90% over a period of about 1.5 h (Table 2). At an

TABLE 1. Leg-averaged altitude, age, temperature, total concentration N, IWC, RH, r_e, and visible extinction coefficient β_{ext} measured by the NASA WB-57F within the TTC. Legs 1, 2, and 3 were flown across wind while the anvil beneath the TTC was still forming. Legs 5 and 9 and legs 6 and 8 were flown along axis. Age is calculated relative to the time of initial detrainment of the anvil proper from the convective updraft. Standard deviations in the measurements are shown in parentheses. Average values below the detection threshold are indicated by an em dash. IWC, β_{ext}, and r_e were measured by CIN and Harvard water probes.

	Across TTC axis			Along TTC axis			
Leg	1	2	3	5	9	6	8
Alt (km)	14.7	14.1	13.5	14.1	14.1	13.5	13.5
Age (min)				74	126	92	116
Temperature (°C)	−70	−67	−63	−68	−67	−63	−62
N (cm^{-3})	0.57 (0.54)	10.7 (8.8)	0.40 (0.39)	0.79 (0.53)	0.17 (0.20)	0.59 (0.68)	1.24 (1.10)
IWC (mg m^{-3})	1.6 (1.1)	35 (30)	2.3 (1.2)	1.8 (0.9)	0.5 (0.5)	1.8 (1.6)	4.4 (4.2)
β_{ext} (km^{-1})	0.5 (0.6)	9.0 (7.1)	0.4 (0.5)	0.4 (0.3)	—	0.4 (0.5)	0.8 (1.0)
r_e (μm)	3.8 (2.1)	7.3 (3.4)	5.0 (1.5)	5.9 (1.6)	5.8 (0.8)	5.5 (3.3)	7.4 (2.2)
RH_{ice} (%)	98 (9)	118 (10)	124 (11)	119 (5)	116 (7)	112 (7)	117 (10)

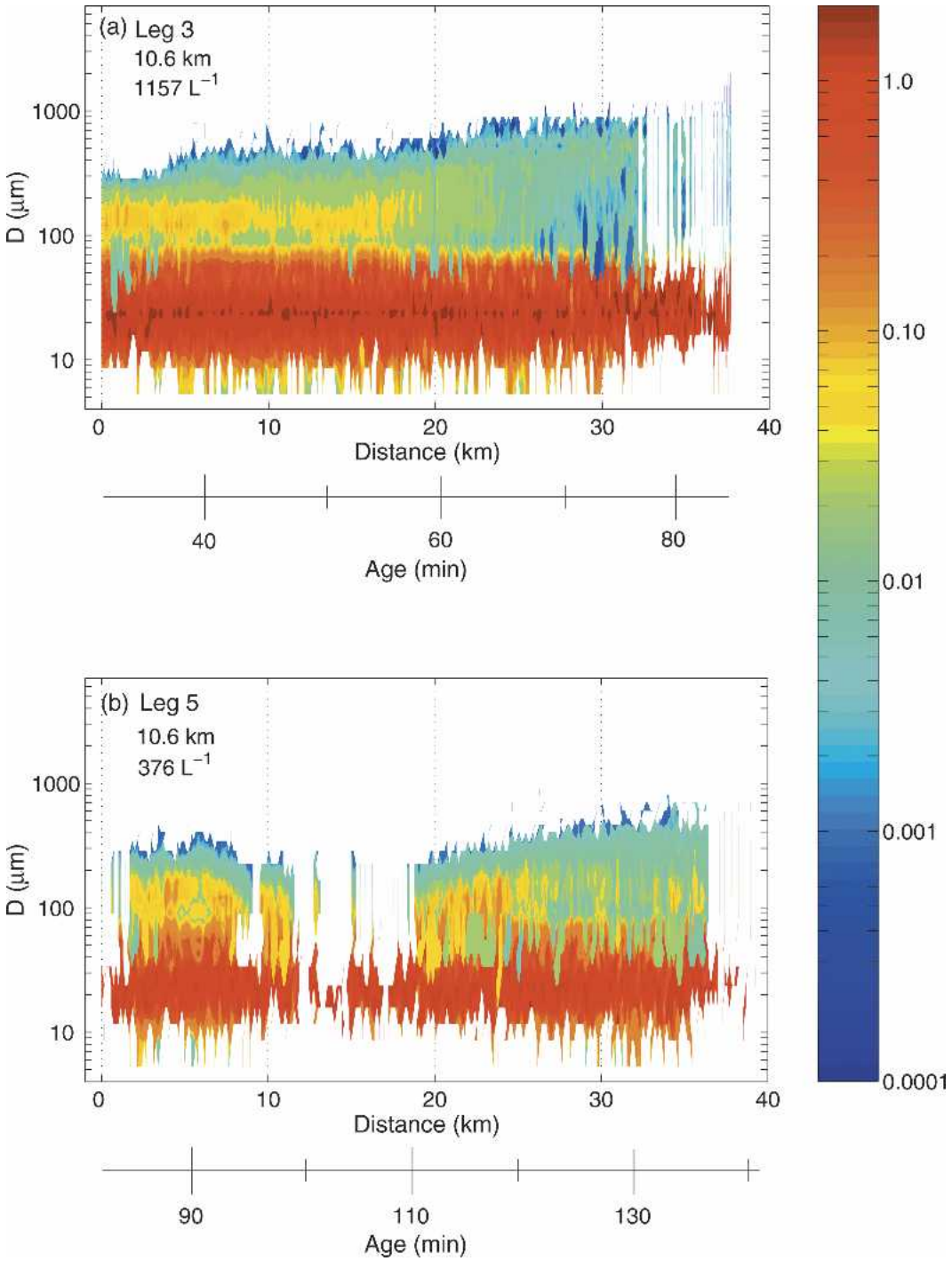

FIG. 9. Normalized ice crystal distributions [$(dN/d\log D)/N$] within the anvil during Citation legs (a) 3 and (b) 5 at 10.6-km altitude. The timeline on the bottom represents the estimated age of cloudy air since initial detrainment from the convective updraft. Average altitude and concentration are shown in the upper-left corner of each plot. Distance is measured from the upwind edge to the downwind edge of the anvil.

altitude of 10.6 km (legs 3 and 5), r_e stayed constant at about 17 μm, while N, IWC, and β_{ext} fell by about a factor of 3 over a period of about 60 min. The relative humidity at each altitude simultaneously decreased by about 10% in each interval, while the temperature remained constant. The total water content (vapor and ice) TWC, which would be a conserved variable in the absence of mixing or precipitation, fell by

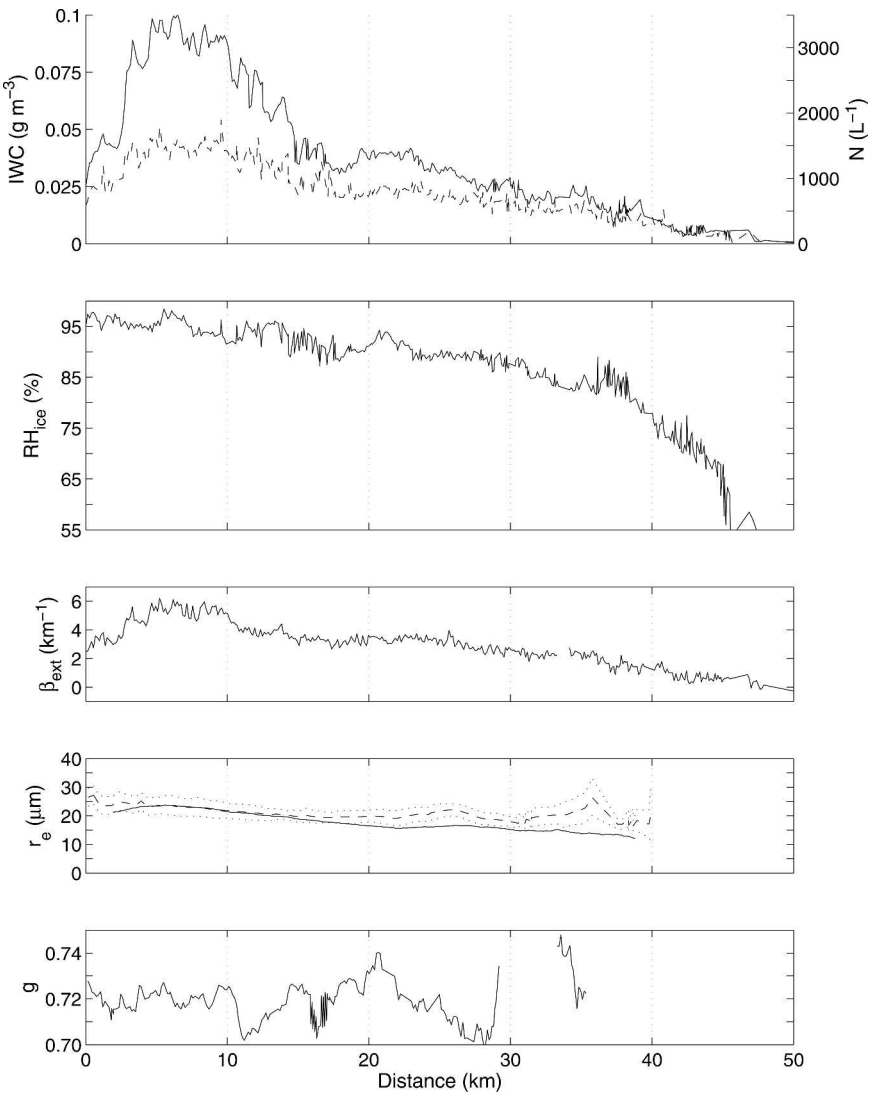

FIG. 10. Citation measurements of anvil IWC (solid line) and ice crystal number concentration N (dashed line), RH_{ice}, β_{ext}, r_e, and g, averaged over legs 1–6 (Fig. 3). *GOES-8* retrievals of r_e [dashed lines with dotted uncertainty; defined according to Eq. (1)] are shown for comparison alongside measured values (solid lines). Distance is referenced from the upwind edge of the anvil.

50% between legs 1 and 6 and by 30% between legs 3 and 5.

5. Radiative fluxes

a. Radiative forcing

We examine the effect of the observed evolution of the anvil microphysical properties on net cloud radiative forcing (CRF_{net}) at the top of the troposphere (TOT) using *GOES-8* imagery, radiometer measurements from the WB-57F during leg 3, and in situ data obtained from the Citation from leg 5. For these two legs the WB-57F and Citation were vertically stacked and close in time and horizontal space. CRF_{net} is defined here as the difference between observed CRF_{obs} and clear-sky CRF_{clr} measurements of the sum of the net longwave and shortwave radiative fluxes, assuming 100% cloud cover. Thus negative (positive) values at the TOT represent a tropospheric cooling (warming) by a cloud.

Radiometer measurements of shortwave and longwave broadband radiative fluxes from leg 5 of the WB-57 were used to calculate TOT CRF_{obs}. This is an imperfect measure because the WB-57F was actually within the TTC cloud layer, rather than above all cloud. However, during leg 5 the WB-57 was at 14.1-km alti-

TABLE 2. Leg-averaged altitude, age, temperature, total concentration N, IWC, RH, total water content (ice plus vapor) TWC, r_e, β_{ext}, and asymmetry parameter g measured by the UND Citation within the anvil. Age is calculated relative to the time of initial detrainment from the convective updraft. Standard deviations in the measurements are shown in parentheses. Average values below the detection threshold are indicated by an em dash.

Leg	1	6	3	5
Alt (km)	11.2	11.2	10.6	10.6
Age (min)	35	123	58	117
Temperature (°C)	−45.3 (0.1)	−44.9 (0.1)	−39.9 (0.2)	−39.5 (0.1)
θ (°C)	70.6	70.8	69.1	69.5
U, V (m s^{-1})	3.8, 4.2	6.2, 6.2	1.8, 2.3	2.3, 3.8
RH_{ice} (%)	101 (8)	92 (6)	104 (5)	93 (8)
TWC (mg m^{-3})	122 (24)	68 (5)	220 (54)	152 (27)
IWC (mg m^{-3})	55 (21)	5 (3)	95 (53)	23 (23)
N (cm^{-3})	1.3 (0.5)	0.23 (0.13)	1.6 (0.6)	0.47 (0.36)
r_e (μm)	12.7 (4.2)	—	17.9 (8.0)	16.8 (7.5)
β_{ext} (km^{-1})	7.1 (2.0)	—	8.6 (3.6)	3.0 (1.6)

tude, in the uppermost part of an already thin TTC layer. Thus any contribution to TOT CRF_{obs} from higher cloud was probably negligible.

Second, although we focus here on radiative forcing by the anvil, the TTC contributes to TOT forcing itself. The magnitude of this effect is addressed later.

Values of CRF_{clr} used to calculate CRF_{net} from CRF_{obs} were estimated by interpolating between WB-57F radiometer measurements obtained in clear sky. Times when the WB-57F was over clear skies (i.e., IWP = 0) were identified from *GOES-8* retrievals taken along the aircraft flight track.

The trends in radiative forcing downwind along the length of the anvil were estimated by taking in situ measurements of IWC and r_e from within the anvil and TTC as inputs to the Streamer radiative transfer model (Key and Schweiger 1998). Although Streamer has a more limited infrared wavelength resolution than many other band models that focus on gases, it allows the user to explicitly define multiple cloud layers with unique values of effective radius, ice water content, and ice crystal habit. A phase function representative of idealized "rough aggregates" ice crystals was assumed here (Yang and Liou 1998) because it corresponds to values of the asymmetry parameter similar to those actually measured in the anvil.

Instantaneous radiative fluxes were calculated for the time and date of the flight legs using the Streamer discrete ordinates solver. Here, we adopted four streams for shortwave and two streams for infrared calculations. Atmospheric profiles were based on those shown in Fig. 2f. The anvil cloud top and vertical dimensions, and the IWC and r_e of the TTC were defined in the model consistent with the measurements shown in Fig. 4f and Fig. 5f.

For these specifications, TOT CRF_{net} for the anvil-TTC system was then calculated for a wide range of values of anvil IWP and r_e. Superimposed on the resulting contour plot (Fig. 11), the trend in CRF_{net} along the length of the anvil is determined in two ways.

In the first approach, CRF_{net} is found from Fig. 11 based on in situ trends in anvil r_e and anvil IWC measured aboard the Citation during leg 3. To obtain CRF_{net} requires assuming a value for cloud thickness in order to convert measured IWC to IWP. To do this we take *GOES-8* retrievals of IWP from where the Citation was at the anvil's upwind edge and compare this

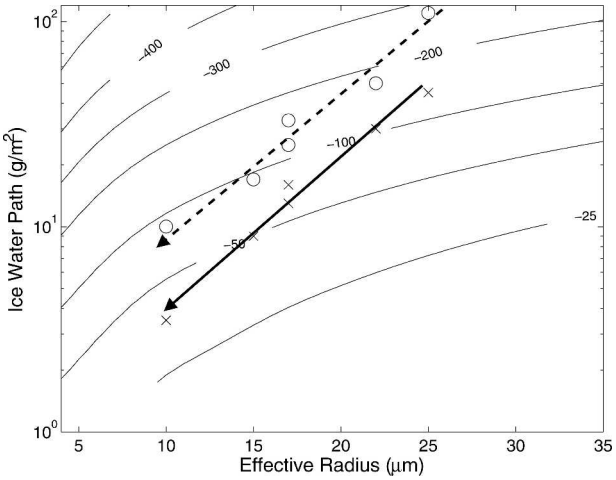

FIG. 11. TOT CRF_{net} calculated for the 21 Jul anvil–TTC system at 2024 UTC (contours, W m^{-2}) as a function of the IWP and effective radius of the anvil. The dashed arrow represents the calculated CRF_{net} trend when using only the in situ anvil r_e and anvil IWC measurements (circles) from the Citation (leg 3), assuming a cloud depth of 500 m. The solid arrow represents the measured CRF_{net} trend when using only the measured CRF_{net} from the WB-57F (leg 5) and in situ anvil r_e (crosses; Citation leg 3). For each case, symbols are separated by 5 km of horizontal flight.

with the in situ measurement of IWC. Since the satellite IWP was approximately 100 g m^{-2} and the aircraft measured IWC was about 0.2 g m^{-3}, we infer that the cloud thickness Δz during Citation leg 3 was 500 m. Thus, the anvil had thinned rapidly since the airborne profile an hour earlier when Δz was 2.5 km and the anvil was still attached to the convection.

We have confidence that this estimate of Δz is fairly accurate for two reasons. First, at the time of the airborne vertical profile, both *GOES-8* retrievals and vertically integrated in situ measurements of IWC showed the anvil IWP was ~250 g m^{-2}. (During the profile, satellite retrieved IWP was derived from an average over a box enclosing the spiral flight path during a series of three *GOES-8* images during the time period of the spiral. This method was chosen because aircraft measurements are continuous within an evolving cloud, while satellite images are snapshots taken every 10 min.) Second, in practice, retrievals of IWP are inferred from retrievals of τ and r_e. Although we cannot validate τ for flight transects, Fig. 10 shows in situ and retrieved r_e were in closest agreement at the upwind edge of the anvil cirrus.

In the second approach for deriving trends in CRF_{net} (Fig. 11), Citation measurements of anvil r_e were combined with nearly simultaneous WB-57F measurements of CRF_{net} from above the anvil-TTC system. For the calculations, the TTC was assumed to have a fixed visible optical depth of 0.3, and an effective radius of 9 μm.

Comparison of these two approaches does not represent a closure study between modeled and measured fluxes. In fact, the WB-57F and Citation aircraft were horizontally separated by about 15 km. Second, both approaches employ in situ measurements of r_e. However, the comparison is useful for corroborating *trends* in net forcing by the TTC-anvil system as it evolves.

The two approaches show close agreement. They show a trend toward less tropospheric cooling along the downwind length of the anvil-TTC system. Precipitation depletes IWP, while simultaneously decreasing r_e. The reduction in r_e slows the warming trend, but it is the trend in IWP that dominates CRF_{net}.

Although, Fig. 11 focuses on TOT CRF_{net} by the anvil, it would be interesting to estimate the effect the presence of the TTC on the calculations, particularly considering a multilayered structure is not typically assumed in calculations of the radiative effects of anvil cirrus.

To estimate this effect, we ran the above calculations with the TTC removed from the atmospheric profile, and then subtracted the resulting TOT CRF_{net} from the results shown in Fig. 11. Values of r_e and IWP obtained from measurements in the anvil are superimposed on the calculated difference (Fig. 12).

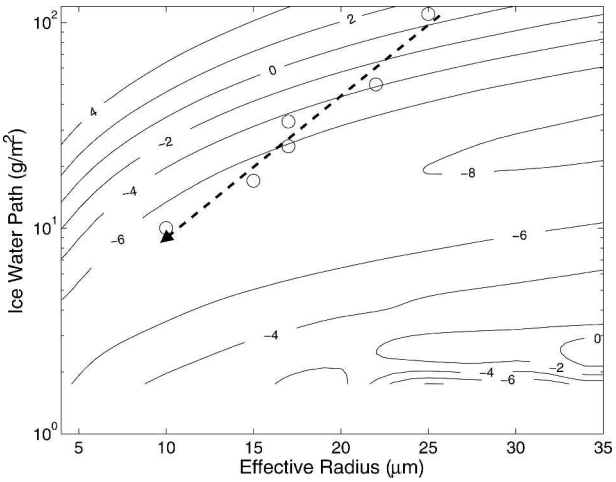

FIG. 12. As in Fig. 11, but for the contribution of the TTC cloud to total forcing by the TTC–anvil system.

The results show that the TTC had no impact on TOT radiative forcing by the anvil when it was thick. However, once the anvil IWP had thinned to 10 g m^{-2}, at which point it was no longer a blackbody, the TTC contributed -7 W m^{-2} to total forcing by the anvil-TTC system, which is about 10% of the total.

In the assumed absence of an anvil beneath the TTC, calculated radiative forcing by the TTC alone at 2024 UTC would have been -15 W m^{-2}.

b. Radiative heating

Since the TTC had a visible optical depth of just ~0.3 (Fig. 5), in an otherwise cloudless sky it would be strongly heated from below. Such heating would be expected to either loft the cloud layer or rapidly dissipate the cloud (Jensen et al. 1996). This was not observed. Rather, the TTC settled and was microphysically very stable. Here we explore a hypothesis of Hartmann et al. (2001) that the TTC might cool because of the presence of an anvil below. Effectively, graybody TTC equilibrates not to the earth's surface but to the anvil, which is much colder. Such cooling might sustain the TTC.

For the case presented here, the TTC was directly situated above the anvil and had similar horizontal dimensions (Garrett et al. 2004). Based on the radiative transfer calculations presented above, in the absence of the anvil, estimated heating rates $\mathcal{H}$ in the TTC would have been 5 K day^{-1}. In its presence, calculated heating rate profiles are shown in Fig. 13. For a thick anvil still attached to the convective core (e.g., $\Delta z = 2.5$ km, $\tau = 21$, and $r_e = 20$ μm), the calculated TTC cooling rate is about 0.2 K day^{-1}. For a thin detached anvil, with

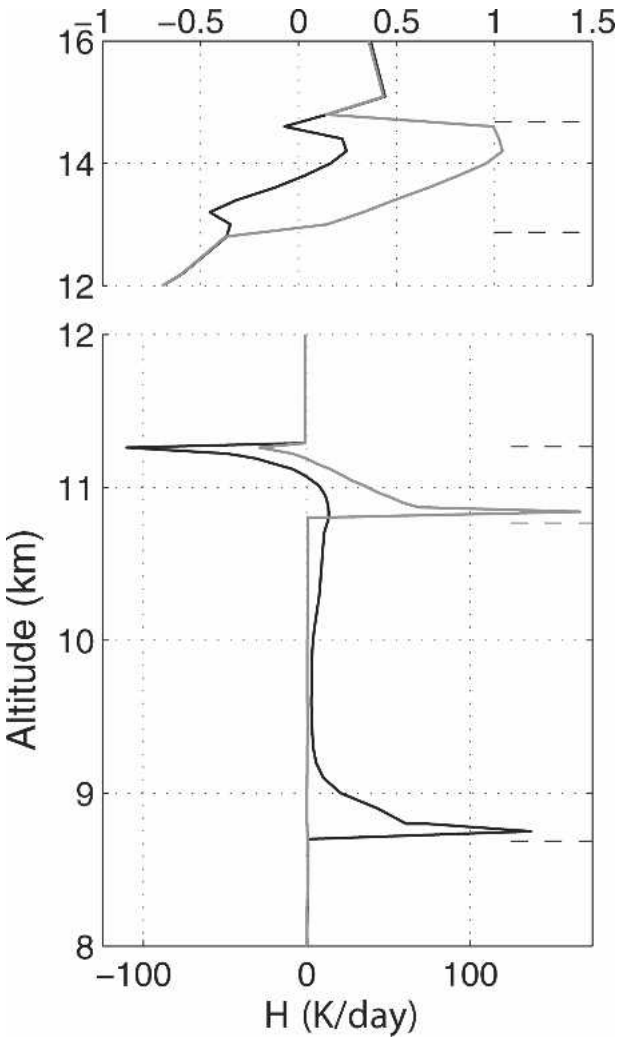

FIG. 13. Calculated heating-rate profiles for an anvil attached to the convective core ($\tau = 21$ and $r_e = 20$ μm; black line) and for thin anvil cirrus detached from the core ($\tau = 2$ and $r_e = 12$ μm; gray). Dashed lines indicate cloud boundaries of the (top) TTC and (bottom) anvil.

$\Delta z = 0.5$ km, $\tau = 2$ with $r_e = 12$ μm, the TTC heated by about 1 K day^{-1}. For a similar cloud scenario observed over the tropical western Pacific Ocean, Comstock et al. (2002) calculated heating rates in the TTC of 0.53 K day^{-1}, mostly due to IR heating.

If, for the sake of argument, no anvil was present below the TTC, the heating rate would have been about 7 K day^{-1}. Therefore, as suggested by Hartmann et al., it appears that the TTC lifetime was prolonged by the anvil's presence. Unfortunately, no measurements were made of the TTC once the anvil had fully dissipated. However, Comstock et al.'s observations of tropical TTC showed that, even once a cirrus anvil has dissipated, TTC layers might persist for several days. Comstock et al. suggested that some other unknown mechanism must protect the cloud from evaporation, even when it is not shielded by an anvil beneath.

The anvil is principally characterized by concentrated heating at the anvil base and cooling at the anvil top (Fig. 13). While the anvil is strongly heated by terrestrial radiation from below, it radiates strongly through its top to outer space. Smaller heating rates in the anvil interior are due to solar heating. As the anvil evolves, its base rises and it becomes less opaque to thermal radiation. The anvil top is then no longer shielded by the anvil interior from terrestrial heating. The anvil heating profile then becomes progressively asymmetric, with more pronounced heating at the bottom than the top of the anvil. At the anvil base, peak $\mathcal{H}$ increases from about 125 K day^{-1} when the anvil is thick and attached to the convective core, to 150 K day^{-1} when it is thinner and detached from the convective core. Simultaneously, at cloud top, peak cooling decreases from 100 to 25 K day^{-1}.

The vertical distribution of heating is less uniform than described in Ackerman et al.'s (1988) description of heating rates in tropical anvils because (a) the anvil top is about 25°C warmer than the tropopause temperature, and (b) the ice crystals have smaller effective radii, making them more efficient absorbers of infrared radiation. The implications of these profiles for the anvil's dynamic evolution are discussed in section 6c.

6. Discussion

a. Small ice crystals

The anvil and TTC shown in this study had high concentrations of small nonprecipitating ice crystals. Although similarly small crystals have been sampled in anvil and midlatitude cirrus elsewhere (e.g., Heymsfield and McFarquhar 1996; Ström et al. 1997) and were observed in all other anvil and TTC clouds sampled during CRYSTAL-FACE (Garrett et al. 2003), their presence in high concentrations remains contentious; it is often argued that the probes usually used to measure these ice crystals artificially inflate the concentrations of small ice crystals because of shattering on the instrument inlet (Gardiner and Hallett 1985; Gayet et al. 1996).

On the other hand, bulk cloud probes measuring cloud mass and optical extinction during CRYSTAL-FACE should be insensitive to ice crystal breakup. IWC remains conserved under crystal disintegration. Extinction would be inflated by breakup, but the CIN probe used to measure optical extinction has no inlet but rather has a broad and aerodynamic aperture rela-

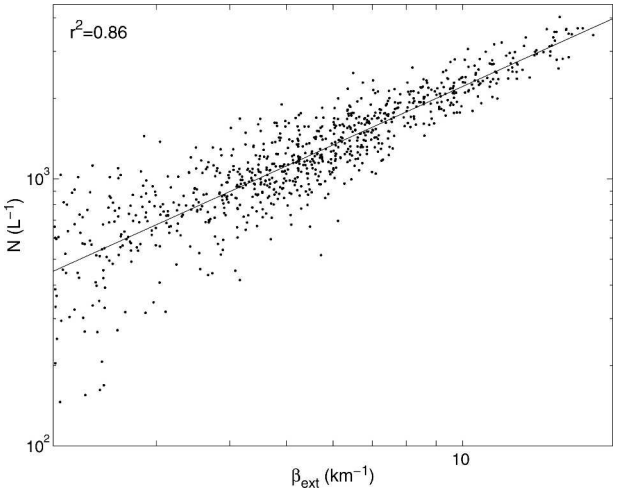

FIG. 14. One-hertz measurements of β_{ext} and N for all six Citation legs through the anvil. The solid line is the least squares fit $N = 227\beta_{ext}^{0.99}$.

tive to both the width of the measurement laser beam and the sizes of large ice crystals.

For each flight leg within the anvil, the effective diameter D_e (2 times the effective radius), derived with bulk cloud probe data from Eq. (1), decreased from approximately 45 μm near the upwind edge of the anvil to approximately 25 μm near the anvil's downwind edge. Within the TTC, measured D_e was approximately 10–20 μm independent of cloud age or distance downwind.

These calculated values of D_e correspond well to the location of the cloud mode in the measured ice crystal size distributions, especially in the downwind region of the anvil where precipitation ice crystals were largest, but in the lowest concentrations. Because large irregular ice crystals were observed in the anvil and, to a lesser extent, in the TTC, inflated concentrations of small particles due to ice crystal shattering cannot be ruled out. However, the consistency between bulk and size distribution measurements suggests this effect was probably small.

In addition, N and β_{ext} for all Citation legs were highly linearly correlated, with a slope of 227 km L^{-1} (Fig. 14). In general, β_{ext} and N are related by

$$\beta_{ext} \simeq \frac{\pi}{2} N\overline{D}^2. \quad (2)$$

From the data shown in Fig. 14, $\overline{D} \simeq 37$ μm, which is in between the values of D_e measured at the upwind and downwind edges of the anvil (Fig. 10). Thus, in contrast to the findings of Heymsfield et al. (1998), small ice crystals appear to have made an important contribution the anvil radiative properties.

b. Microphysical evolution

A full understanding of the evolution of a cirrus anvil requires a detailed model with coupled dynamics, radiation, and microphysics. Here we describe the mechanisms controlling the evolution of the 21 July anvil based on an interpretation of the previously described observations and calculations.

The anvil became progressively subsaturated with distance downwind from its upwind edge (Fig. 10). It has been argued that most anvil ice crystals form from homogeneous freezing of haze particles entrained into convective updraft cores (Fridlind et al. 2004). Once ejected from the convection, their exposure to subsaturated conditions in the anvil might be expected to result in a shift of the measured cloud mode to smaller sizes as the anvil evolved. For example, given the humidity conditions observed during Citation leg 5 (Table 2), the time scale for a 20-μm crystal to sublimate to 10 μm is about 1 min.

However, anvil ice crystal size distributions (Fig. 9) show no correspondence between the age of the air parcel and the size of the cloud mode ice crystals. This is surprising, and it is unclear how the small mode of the size distribution can be maintained under subsaturated conditions. Possible explanations include the following: 1) Large crystals were in fact breaking up in the FSSP-100 inlet, which may have masked any such shift. However, as discussed in section 6a, it seems unlikely from bulk probe data that such breakup was in fact significantly affecting measured size distributions. 2) As aggregate ice crystals evaporate, they may break-up to maintain a small particle mode (Bacon et al. 1998). 3) Small crystals might be replenished by small-scale updrafts carrying crystals from subsaturated regions below the Citation flight level (Zender and Kiehl 1994). This can occur if large ice crystals below cloud base shrink due to evaporation, and then are subsequently lofted back into the anvil. 4) It may be that complete evaporation is occurring, but in subsaturated pockets smaller than the spatial resolution of the aircraft measurements. In such case, measured RH, N, and IWC might decrease as the anvil evolves, but without any apparent shrinkage of ice crystals. 5) Ice crystals are regenerated at the anvil base from haze particles and subsequently lofted upward by internal circulations in the anvil.

Large aggregates increased in size and concentration between the upwind and downwind edges of the anvil (the precipitation mode in Fig. 9a). This shift in the precipitation mode with distance downwind from the anvil's upwind edge disappeared by the time the anvil aged an additional hour (Fig. 9b). What appears to have

occurred is that, in the 40-min evolution that separated the downwind from the upwind edge of the anvil, ice crystals ejected from the convective core aggregated further in the anvil, and their maximum dimension increased by a factor of ~4 while their concentration decreased by a factor of ~10. Large aggregates settled quickly, at a rate of ~1 m s^{-1} (Heymsfield et al. 2002), and although internal circulations in the anvil may have slowed their descent, they were removed rapidly from the anvil plume as precipitation, further aggregating on their way to cloud base. The very largest aggregates (>1000 μm across) were only observed at the very lowest levels of the anvil and at the earliest stages of anvil detrainment (Fig. 4b).

Over the course of about an hour, TWC in the anvil fell by ~0.06 g m^{-3} (Table 2). Assuming mass and fall speed relationships for the measured size distributions of precipitating ice crystals that are suitable for aggregates of side planes (Heymsfield et al. 2002) and assuming an anvil thickness of 1 km, the approximate loss rate of TWC and IWC from precipitation was 0.05 g m^{-3} h^{-1}. Therefore, the anvil is quickly dessicated by the settling of ice crystal aggregates.

c. Dynamical evolution

Thermodynamically, the temperature and stratification of the anvil stayed nearly constant despite strong calculated radiative heating gradients. Based on the measured differences in θ between 10.6- and 11.2-km altitude (Table 2), the anvil stratification $d\theta/dz$ was about 2.2 K km^{-1}. Similar stratification was measured during the initial profile of the anvil and also in surrounding ambient air (Fig. 2).

Based on the in situ meteorological data obtained during the Citation profile of the anvil, the bulk Richardson number Ri for the entire anvil layer was approximately 5. At ages of about 0.75 and 2 h, Ri was about 3 and 1, respectively (Table 2). These values are larger than the critical value (Ri_{crit}=0.25) below which it is usually assumed that turbulence is sustained. Because of sporadic performance of the gust probe, no vertical profile was obtained of the buoyancy flux in the anvil. However, no vigorous updrafts were measured. The standard deviation of the updraft velocity measured by the Citation at 10.6-km altitude (legs 3 and 5) was 0.25 m s^{-1}.

Discussions of the dynamical evolution of anvil layers (Ackerman et al. 1988; Lilly 1988) often assume that net heating of the layer drives the cloud as a whole vertically upward. Strong negative heating gradients in the cloud drive convection and maintain an adiabatic lapse rate within the cloud. If the anvil precipitates, the radiative heating provides for a "dehydration engine" that plausibly accounts for observations of lower-than-expected humidities in the lower stratosphere (Danielsen 1982).

The measurements presented here show that in fact the anvil temperature was stable. Second, the stratification of the cloud stayed nearly identical to that of its environment and the Richardson number for the layer was high. Thus, it seems worth considering whether, instead of driving turbulent mixing throughout the entire depth of the layer, cooling at cloud top and heating at cloud base drove horizontal motion instead, so that vertical stratification in the anvil was maintained.

Consider Fig. 13, where the anvil interior was radiatively shielded by strongly absorbing/emitting layers at the anvil base and top. Because the ice crystals are generally small and have high specific absorption, the heating is concentrated rather than linearly distributed (Lilly 1988).

There are two possible scenarios for how such heating might drive spreading. In the first, potential temperature surfaces are assumed to stay flat. Then, in the absence of horizontal temperature gradients or heating in the anvil, the vertical velocity component for the radiatively interacting layers is given simply by $w_{strat} = \mathcal{H}/(d\theta/dz)$. The top of the cloud sinks and the bottom rises in response to the heating. The cirrus just thins and spreads. The rate of spreading of the radiative layer away from the horizontal center of the anvil cirrus is given by the continuity equation and by scale analysis would have been of order $u_{strat} \sim Lw_{strat}/h$, where L is the half-width of the anvil and h is the penetration depth of infrared radiation into the cirrus. Note that h does not increase greatly as the anvil evolves because, at the same time the cloud loses mass, r_e gets smaller, and the existing mass absorbs/emits thermal radiation more effectively. In this scenario, spreading of the anvil involves associated inertial accelerations that require horizontal pressure gradients. The spreading velocity u_{strat} is then the speed required for no major disruption to surfaces of constant potential temperature.

A second scenario is that strong radiative heating or cooling in the radiative layers may have caused a depth h at the cloud top and bottom to become well mixed while the cirrus interior stayed stratified. In this case, horizontal gradients in θ are produced, and these cause the mixed layers to spread laterally as density currents with a speed $u_{mix} \sim Nh$ (Scorer 1978), where in this case N is now the buoyancy frequency of the environment.

Thus one can imagine a dimensionless number S that expresses the relative importance of these two mechanisms to anvil spreading

$$S = \frac{u_{\text{strat}}}{u_{\text{mix}}} = \frac{\mathcal{H}L}{Nh^2(d\theta/dz)}.$$

When $S \gg 1$, u_{strat} is much greater than u_{mix} and the second scenario dominates: any pressure perturbation due to heating preferentially drives mixing at the boundaries rather than stratified ascent. The converse applies when $S \ll 1$. Assuming characteristic values for N ($\sim$0.01 s^{-1}), $\mathcal{H}$ (50 K day^{-1}), L ($\sim$10 km), $d\theta/dz$ (2 K km^{-1}), and h ($\sim$100 m), we estimate $S \sim 20$. Thus the anvil spreads at a rate $u_{\text{mix}} \sim 1$ m s^{-1} because concentrated radiative heating creates density currents of depth h that are composed of well-mixed cold and warm air and that push laterally into their environment. This estimate for u_{mix} is approximately consistent with satellite imagery, which showed that the detached anvil spread to either side of its center at a rate of $\sim$2 m s^{-1} (Figs. 1c,d).

The frontal mechanism proposed presumes that only the upper and lower bounds of the cloud become well-mixed, and that the energy associated with heating drives lateral spreading rather than vertical motion throughout the entire cloud layer. Well-mixed layers were not in fact observed. It is possible they merely escaped notice because the Citation aircraft did not adequately profile these portions of the cloud. We intend to explore this issue further by investigating temperature profiles of spreading anvil cirrus measured on other days during CRYSTAL-FACE.

7. Conclusions

We have presented here in situ measurements of cloud microphysical and single-scattering properties within an evolving cirrus anvil observed west of south Florida on 21 July 2002. The anvil detrained from a relatively weak storm that developed along a sea-breeze front and was isolated from other convective cells. The anvil was well characterized by two aircraft over a period of 3 h, which made it an ideal candidate for case study. While the convective core of the storm moved eastward, the anvil developed in northeasterly flow and spread over the Gulf of Mexico. From this study we have come to the following conclusions.

1) As with many other anvils observed during CRYSTAL-FACE (Garrett et al. 2004), the anvil had two distinct layers. Separated vertically from an optically thick anvil layer by 1.5 km was a second cloud layer distributed equally between the upper troposphere and lower tropopause. This second layer was termed thin tropopause cirrus. Although 1.5 km thick, it was extremely tenuous, with IWC values of about 1 mg m^{-3} and a visible optical depth of just $\sim$0.3. The size distribution was characterized by a single mode of small ice crystals with an effective radius of 4–10 μm. The microphysical properties of the TTC were quasi steady over the sampling period. This might be because, as pointed out by Hartmann et al. (2001) and confirmed in radiative transfer calculations presented here, a lower anvil layer can shield the TTC from the intense flux of infrared radiation from the surface. If the anvil is thick, the TTC cools. Garrett et al. (2004) hypothesized that TTC originate as convectively forced pileus clouds, spreading as buoyancy waves near the tropopause. Plausibly, over low-latitudes these TTC might be common and might evolve to become the widespread subvisible cirrus apparently centered around tropical convection (Pfister et al. 2001; Dessler and Yang 2003).
2) In the anvil layer itself, the ice crystal size distribution was bimodal. In its early stages, it was characterized by a cloud mode centered at 30-μm maximum dimension and a precipitation mode composed of aggregate ice crystals. The location of this mode was centered at about 150-μm maximum dimension at the anvil's leading edge; at the anvil's trailing edge 30 km downwind, this mode shifted to 700-μm maximum dimension. At the same altitude, almost an hour later, this size shift was no longer observed because the largest ice crystals had precipitated.
3) Concentrations of crystals in the cloud mode were up to 1000 times those in the precipitation mode. These small crystals dominated the anvil radiative properties, particularly at the downwind edge of the anvil where large ice crystals had precipitated. Ice crystal effective radii r_e decreased from 20 to 12 μm as the anvil evolved.
4) In 2 h from when the anvil detached from the convective core, the anvil IWC fell from 0.3 to 0.01 g m^{-3}. This was primarily due to precipitation, but evaporation may have also played an important role. At the same time the cloud thinned from a depth of about 2.5 to 0.5 km.
5) The instantaneous net top-of-troposphere radiative forcing was strongly cooling at the anvil leading edge but tended toward zero as the anvil thinned downwind. While the decrease in IWP dominated this trend, it was slowed by the simultaneous decrease in r_e. The TTC made a negligible contribution to the overall forcing by the cloud system except when the anvil became highly transparent.
6) Because small ice crystals dominated the anvil radiative properties, absorption/emission of radiation by the anvil cirrus was concentrated in the top and bottom 100 m of the cloud while the interior was

largely shielded from rapid heating. Like its environment, the cloud maintained a stratification of about 2 K km^{-1}. This was despite the rapid cooling (heating) at cloud top (bottom), which might normally be assumed to make the anvil cirrus well mixed. We argue that, rather than driving convection through the entire layer, the concentrated interaction with thermal radiation at the cloud vertical boundaries created thin frontal tongues that spread the anvil cirrus laterally while leaving the stability of the interior intact.

Acknowledgments. This work was supported by the NASA CRYSTAL-FACE project. We appreciate stimulating discussions about the dynamics of fluids and clouds with C. Garrett and S. Krueger, a helpful review from D. Wilson, and efforts of the flight crews of the NASA WB-57F and University of North Dakota Citation during CRYSTAL-FACE.

REFERENCES

Ackerman, T. P., K.-N. Liou, F. P. J. Valero, and L. Pfister, 1988: Heating rates in tropical anvils. *J. Atmos. Sci.,* **45,** 1606–1623.

Bacon, N. J., B. D. Swanson, M. B. Baker, and E. J. Davis, 1998: The breakup of levitated frost particles. *J. Geophys. Res.,* **103,** 13 763–13 775.

Baumgardner, D., H. Jonsson, W. Dawson, D. O'Connor, and R. Newton, 2002: The cloud, aerosol and precipitation spectrometer (CAPS): A new instrument for cloud investigations. *Atmos. Res.,* **59–60,** 251–264.

Buck, A., 1985: The lyman-alpha hygrometer. *Moisture and Humidity, 1985: Measurement and Control in Science and Industry: Proceedings of the 1985 International Symposium on Moisture and Humidity*, Washington, DC, Instrument Society of America, 411–436.

Comstock, J. M., T. P. Ackerman, and G. G. Mace, 2002: Ground-based lidar and radar remote sensing of tropical cirrus clouds at Nauru Island: Cloud statistics and radiative impacts. *J. Geophys. Res.,* **107,** 4714, doi:10.1029/2002JD002203.

Danielsen, E. F., 1982: A dehydration mechanism for the stratosphere. *Geophys. Res. Lett.,* **9,** 605–608.

Dessler, A. E., and P. Yang, 2003: The distribution of tropical thin cirrus clouds inferred from *Terra* MODIS data. *J. Climate,* **16,** 1241–1247.

Foot, J. S., 1988: Some observations of the optical properties of clouds, Part 2, Cirrus. *Quart. J. Roy. Meteor. Soc.,* **114,** 145–164.

Fridlind, A. M., and Coauthors, 2004: Evidence for the predominance of mid-tropospheric aerosols as substropical anvil cloud nuclei. *Science,* **304,** 718–722.

Gardiner, B. A., and J. Hallett, 1985: Degradation of in-cloud forward scattering spectrometer probe measurements in the presence of ice particles. *J. Atmos. Oceanic Technol.,* **2,** 171–180.

Garrett, T. J., P. V. Hobbs, and H. Gerber, 2001: Shortwave, single-scattering properties of arctic ice clouds. *J. Geophys. Res.,* **106,** 15 155–15 172.

——, H. Gerber, E. M. Weinstock, C. H. Twohy, and D. G. Baumgardner, 2003: Small, highly reflective ice crystals in low-latitude cirrus. *Geophys. Res. Lett.,* **30,** 2132, doi:10.1029/2003GL018153.

——, A. J. Heymsfield, M. J. McGill, B. A. Ridley, D. G. Baumgardner, T. P. Bui, and C. R. Webster, 2004: Convective generation of cirrus near the tropopause. *J. Geophys. Res.,* **109,** D21203, doi:10.1029/2004JD004952.

Gayet, J.-F., G. Febvre, and H. Larsen, 1996: The reliability of the PMS FSSP in the presence of small ice crystals. *J. Atmos. Oceanic Technol.,* **13,** 1300–1310.

Gerber, H., Y. Takano, T. J. Garrett, and P. V. Hobbs, 2000: Nephelometer measurements of the asymmetry parameter, volume extinction coefficient, and backscatter ratio in Arctic clouds. *J. Atmos. Sci.,* **57,** 3021–3034.

Griffith, K. T., S. K. Cox, and R. G. Knollenberg, 1980: Infrared radiative properties of tropical cirrus clouds inferred from aircraft measurements. *J. Atmos. Sci.,* **37,** 1077–1087.

Hartmann, D. L., J. R. Holton, and Q. Fu, 2001: The heat balance of the tropical tropopause, cirrus, and stratospheric dehydration. *Geophys. Res. Lett.,* **28,** 1969–1972.

Heymsfield, A. J., 1986: Ice particle evolution in the anvil of a severe thunderstorm during CCOPE. *J. Atmos. Sci.,* **43,** 2463–2478.

——, and G. M. McFarquhar, 1996: High albedos of cirrus in the tropical Pacific warm pool: Microphysical interpretations from CEPEX and from Kwajalein, Marshall Islands. *J. Atmos. Sci.,* **53,** 2424–2451.

——, ——, W. D. Collins, J. A. Goldstein, F. P. J. Valero, W. Hart, and P. Pilewskie, 1998: Cloud properties leading to highly reflective tropical cirrus: Interpretations from CEPEX, TOGA COARE, and Kwajalein, Marshall Islands. *J. Geophys. Res.,* **103,** 8805–8812.

——, S. Lewis, A. Bansemer, J. Iaquinta, L. M. Miloshevich, M. Kajikawa, C. Twohy, and M. Poellot, 2002: A general approach for deriving the properties of cirrus and stratiform ice cloud particles. *J. Atmos. Sci.,* **59,** 3–29.

Iacobellis, S. F., and R. C. J. Somerville, 2000: Implications of microphysics for cloud-radiation parameterizations: Lessons from TOGA COARE. *J. Atmos. Sci.,* **57,** 161–183.

Jensen, E. J., O. B. Toon, H. B. Selkirk, J. D. Spinhirne, and M. R. Schoeberl, 1996: On the formation and persistence of subvisible cirrus clouds near the tropical tropopause. *J. Geophys. Res.,* **101,** 21 361–21 375.

Key, J., and A. J. Schweiger, 1998: Tools for atmospheric radiative transfer: Streamer and FluxNet. *Comput. Geosci.,* **24,** 443–451.

Khelif, D. S., S. P. Burns, and C. A. Friehe, 1999: Improved wind measurements on research aircraft. *J. Atmos. Oceanic Technol.,* **16,** 860–875.

Knollenberg, R. G., A. J. Daschler, and D. Huffman, 1982: Measurements of the aerosol and ice crystal populations in tropical stratospheric cumulonimbus anvils. *Geophys. Res. Lett.,* **9,** 613–616.

——, K. Kelley, and J. C. Wilson, 1993: Measurements of high number densities of ice crystals in the tops of tropical cumulonimbus. *J. Geophys. Res.,* **98,** 8639–8664.

Koop, T., B. Luo, A. Tsias, and B. Peter, 2000: Water activity as the determinant for homogeneous ice nucleation in aqueous solutions. *Nature,* **406,** 611–614.

Lawson, R. P., B. A. Baker, C. G. Schmitt, and T. L. Jensen, 2001: An overview of microphysical properties of Arctic clouds observed in May and July during FIRE ACE. *J. Geophys. Res.,* **106,** 14 989–15 014.

Li, Y., 2003: Intensity of convective storms in Florida and their environmental properties. M.S. thesis, Dept. of Meteorology, University of Utah, 116 pp.

Lilly, D. K., 1988: Cirrus outflow dynamics. *J. Atmos. Sci.,* **45,** 1594–1605.

Macke, A., 1993: Scattering of light by polyhedral ice crystals. *Appl. Opt.,* **32,** 2780–2788.

May, R. D., 1998: Open-path, near-infrared tunable diode laser spectrometer for atmospheric measurements of H_2O. *J. Geophys. Res.,* **103,** 19 161–19 172.

McFarquhar, G. M., and A. J. Heymsfield, 1997: Parameterization of tropical cirrus ice crystal size distributions and implications for radiative transfer: Results from CEPEX. *J. Atmos. Sci.,* **54,** 2187–2200.

Minnis, P., and Coauthors, 1995: Cloud optical property retrieval (subsystem 4.3). Clouds and the Earth's Radiant Energy System (CERES) Algorithm Theoretical Basis Document, Volume III: Cloud Analyses and Radiance Inversions (Subsystem 4), NASA Rep. 1376, CERES Science Team, Eds., Vol. 3, NASA, 135–176.

——, D. P. Garber, D. Young, R. F. Arduini, and Y. Takano, 1998: Parameterizations for reflectance and emittance for satellite remote sensing of cloud properties. *J. Atmos. Sci.,* **55,** 3313–3339.

Noone, K. J., J. A. Ogren, J. Heintzenberg, R. J. Charlson, and D. S. Covert, 1988: Design and calibration of a counterflow virtual impactor for sampling for atmospheric fog and cloud droplets. *Aerosol Sci. Technol.,* **8,** 235–244.

Payne, G. A., C. A. Friehe, and D. K. Edwards, 1994: Time and frequency response of a resistance-wire aircraft atmospheric temperature sensor. *J. Atmos. Oceanic Technol.,* **11,** 463–475.

Pfister, L., and Coauthors, 2001: Aircraft observations of thin cirrus clouds near the tropical tropopause. *J. Geophys. Res.,* **106,** 9765–9786.

Scorer, R. S., 1978: *Environmental Aerodynamics.* Ellis Horwood, 488 pp.

Scott, S. G., T. P. Bui, K. R. Chan, and S. W. Bowen, 1990: The Meteorological Measurement System on the NASA ER-2 aircraft. *J. Atmos. Oceanic Technol.,* **7,** 525–540.

Ström, J., B. Strauss, T. Anderson, F. Schröder, J. Heintzenberg, and P. Wendling, 1997: In situ observations of the microphysical properties of young cirrus clouds. *J. Atmos. Sci.,* **54,** 2542–2553.

Twohy, C. H., A. J. Schanst, and W. A. Cooper, 1997: Measurement of condensed water content in liquid and ice clouds using an airborne counterflow virtual impactor. *J. Atmos. Oceanic Technol.,* **14,** 197–202.

Valero, F. P. J., A. Bucholtz, B. C. Bush, S. K. Pope, W. D. Collins, and P. Flatau, 1997: Atmospheric Radiation Measurements Enhanced Shortwave Experiment (ARESE): Experimental and data details. *J. Geophys. Res.,* **102** (D25), 29 929–29 937.

Weinstock, E. M., and Coauthors, 1994: New fast response photofragment fluorescence hygrometer for use on the NASA ER-2 and the Perseus remotely piloted aircraft. *Rev. Sci. Instrum.,* **65,** 3544–3554.

Yang, P., and K.-N. Liou, 1998: Single scattering properties of complex ice crystals in terrestrial atmosphere. *Contrib. Atmos. Phys.,* **71,** 223–248.

Zender, C. S., and J. T. Kiehl, 1994: Radiative sensitivities of tropical anvils to small ice crystals. *J. Geophys. Res.,* **99,** 869–880.